Advance Access publication 2022 March 9

MNRAS 512, 3331-3344 (2022)

Properties of the Be-type stars in 30 Doradus

P. L. Dufton, ¹* D. J. Lennon, ² J. I. Villaseñor ⁶, ³ I. D. Howarth ⁶, ⁴ C. J. Evans, ⁵ S. E. de Mink ⁶, ⁶ H. Sana ¹⁰⁷ and W. D. Taylor⁵

Accepted 2022 March 4. Received 2022 March 4; in original form 2021 October 22

ABSTRACT

The evolutionary status of Be-type stars remains unclear, with both single-star and binary pathways having been proposed. Here, VFTS spectroscopy of 73 Be-type stars, in the spectral-type range, B0–B3, is analysed to estimate projected rotational velocities, radial velocities, and stellar parameters. They are found to be rotating faster than the corresponding VFTS B-type sample but simulations imply that their projected rotational velocities are inconsistent with them all rotating at near critical velocities. The de-convolution of the projected rotational velocities estimates leads to a mean rotational velocity estimate of 320-350 km s⁻¹, approximately 100 km s⁻¹ larger than that for the corresponding B-type sample. There is a dearth of targets with rotational velocities less than 0.4 of the critical velocity, with a broad distribution reaching up to critical rotation. Our best estimate for the mean or median of the rotational velocity is 0.68 of the critical velocity. Rapidly rotating B-type stars are more numerous than their Be-type counterparts, whilst the observed frequency of Be-type stars identified as binary systems is significantly lower than that for normal B-type stars, consistent with their respective radial-velocity dispersions. The semi-amplitudes for the Be-type binaries are also smaller. Similar results are found for a Small Magellanic Cloud Be-type sample centred on NGC 346 with no significant differences being found between the two samples. These results are compared with the predictions of single and binary stellar evolutionary models for Be-type stars. Assuming that a single mechanism dominated the production of classical Be-type stars, our comparison would favour a binary evolutionary history.

Key words: stars: emission-line, Be – stars: rotation – Magellanic Clouds – galaxies: star clusters: individual: Tarantula Nebula.

1 INTRODUCTION

An important subgroup within the B-type stellar population are Be-type stars, which exhibit strong emission in their Balmer lines (Collins 1987; Jaschek & Jaschek 1990). Generally the Be-type classification excludes supergiants, young Herbig stars, mass transfer binaries, and B[e] type stars as discussed by, for example, Rivinius, Carciofi & Martayan (2013). Struve (1931) first identified that Betype stars rotated relatively rapidly and that their emission lines could be ascribed to a circumstellar disc. In our Galaxy, Zorec & Briot (1997) found approximately 17 per cent of B-type stars to be Be-type, with estimates of 17–20 per cent in the Large Magellanic Cloud (Martayan et al. 2006) and 26-40 per cent in the Small Magellanic Cloud (SMC; Martayan et al. 2007b). Martayan et al. (2007a) suggested that the higher percentage for the SMC might be due to systematic larger stellar rotational velocities in this lower metallicity environment.

The rotational velocities of Be-type stars have been studied by many authors with the earlier investigations being critically reviewed by Rivinius et al. (2013). They concluded that Be-type stars typically rotated at a fraction of approximately 0.8 of the Keplerian circular orbital velocity. Subsequently Zorec et al. (2016) studied the rotational properties of a large sample of Galactic Be-type stars. They deconvolved the projected rotational velocities $(v_e \sin i)$ estimates to deduce the underlying distribution of equatorial radial velocities. After carefully considering possible systematic errors in both the $v_e \sin i$ -estimates and stellar parameters, they concluded that the mode of the equatorial rotational velocity as a fraction of the critical velocity was approximately 0.65. Recently Balona & Ozuyar (2020a, b) have discussed TESS photometry of over 400 Galactic Betype stars and deduced their rotational periods and hence equatorial rotational velocities. Their results are in excellent agreement with those of Zorec et al. (2016). These more recent results are difficult to reconcile with all Be-type stars being near critical rotators and indeed Zorec et al. (2016) commented that 'the probability that Be stars are critical rotators is extremely low'

The current evolutionary status of Be-type stars remains unclear, with theoretical models falling into two broad categories, viz. those

¹Astrophysics Research Centre, School of Mathematics and Physics, Queen's University Belfast, Belfast BT7 1NN, UK

²Instituto de Astrofísica de Canarias, E-38200 La Laguna, Tenerife, Spain

³Institute for Astronomy, University of Edinburgh, Royal Observatory, Blackford Hill, Edinburgh EH9 3HJ, UK

⁴Department of Physics and Astronomy, University College London, Gower Street, London WC1E 6BT, UK

⁵UK Astronomy Technology Centre, Royal Observatory Edinburgh, Blackford Hill, Edinburgh EH9 3HJ, UK

⁶Max-Planck-Institut für Astrophysik, Karl-Schwarzschild-Strasse 1, D-85741 Garching, Germany

⁷Institut voor Sterrenkunde, Universiteit Leuven, Celestijnenlaan 200 D, B-3001 Leuven, Belgium

^{*} E-mail: P.Dufton@qub.ac.uk

that postulate that Be-type stars have evolved as single stars or that they are the product of previous mass transfer in a binary system. For the former (which could apply to both single and non-interacting binary systems), the Be-type properties would simply arise from their large rotational velocities relative to their critical velocities. This could be due to high primordial rotational velocities although as discussed by Bodensteiner, Shenar & Sana (2020b) this would appear to be inconsistent with observational studies of stellar rotation rates. Alternatively it could arise from changes in the rotational velocity and the critical velocity as a B-type star evolves from the zero age main sequence. Recently Hastings, Wang & Langer (2020) have discussed this scenario and found that equatorial velocities that are near to critical should occur. However their comparison with the observed properties of Be-type stars highlighted a number of inconsistencies. Additionally their modelling assumed that all rapidly rotating objects would be Be-type stars, whilst as discussed in Section 6.5 this is not the case.

Evolutionary histories involving binary interactions have also been extensively explored (see for example, Pols et al. 1991; de Mink et al. 2013; Rivinius et al. 2013; Shao & Li 2014, 2020; Hastings et al. 2021). In this scenario the observed Be-type star was originally the less massive component and has accreted mass and angular momentum from the more massive primary, which if it does not become a supernova, can evolve into a low mass helium star or white dwarf.

The VLT-FLAMES Tarantula Survey (VFTS) obtained multiepoch optical spectroscopy of over 800 massive stars in the 30 Doradus region (Evans et al. 2011) of which 438 were classified as B-type, including 73 Be-type (Evans et al. 2015). The only selection criterion was a magnitude cut-off at V = 17, in order to provide sufficient signal-to-noise ratios in the spectroscopy. As such it provides a relatively unbiased Be-type sample, together with a comparable B-type sample. Because of the magnitude cut-off, both samples are limited to the earlier B-types, viz B0-B3. Further details of the samples and their biases can be found as supplementary material in Appendix E. Below we analyse these samples to investigate rotational and radial velocities, stellar parameters, and binarity. We also consider comparable samples of Be-type and B-type stars in NGC 346 in the SMC (Dufton et al. 2019). These results are used to address several issues for Be-type stars and in particular their evolutionary status and whether they are all rotating at near critical velocities.

2 OBSERVATIONS

2.1 Target selection and data reduction

The VFTS spectroscopy was obtained using the MEDUSA mode of the FLAMES instrument (Pasquini et al. 2002) on the ESO *Very Large Telescope* and has been discussed in detail by Evans et al. (2011). MEDUSA uses fibres to simultaneously 'feed' the light from over 130 sky positions to the Giraffe spectrograph. Nine fibre configurations (designated fields 'A'-'I' with near-identical field centres) were observed in the 30 Doradus region, sampling different clusters and the local field population. Three standard Giraffe grating settings were used viz. LR02 (wavelength range from 3960 to 4564 Å at a spectral resolving power of $R \sim 7000$), LR03 (4499–5071 Å, $R \sim 85000$), and HR15N (6442–6817 Å, $R \sim 16000$). Spectroscopy of more than 800 early-type stars was obtained with 73 targets subsequently being classified as Be-type by Evans et al. (2015), from the identification of stellar H α emission in HR15N spectroscopy. Details of the target selection, observations, and initial

data reduction have been given in Evans et al. (2011), where target coordinates were also provided. Fig. 1 illustrates the spatial positions of all the Be-type stars that have been analysed.

For the analyses presented, both the LR02 and LR03 spectroscopy was utilized with all useable exposures of a given target being combined (after normalization) using either a median or weighted σ -clipping algorithm. The final spectra from the different methods were normally indistinguishable. The combined spectra for some features (e.g. the Balmer series) were subsequently re-normalized to ensure consistency with the normalizations adopted in the theoretical predictions.

Garland et al. (2017) have discussed the estimation of projected rotational velocities ($v_e \sin i$) for SB1 candidates from spectroscopy that had been combined without wavelength shifts. They concluded that this would not lead to significant errors provided the range of radial velocities (Δv_r) was relatively small. For stars with negligible rotation, the limit was $\Delta v_r \lesssim 30 \text{ km s}^{-1}$, increasing to, for example, 120 km s^{-1} for $v_e \sin i \sim 200 \text{ km s}^{-1}$. All the SB1 candidates considered here fulfil these criteria and therefore no velocity shifts have been applied to exposures at different epochs.

We have searched the Hubble Legacy Archive to search for spatially close companions, with imaging available for over 80 per cent of our sample. Nine targets had possible contamination, with that for four targets (#272, #283, #644, and #824) being potentially serious. Further details can be found in the supplementary material in Appendix A.

2.2 Binarity

Dunstall et al. (2015) identified seven of our targets as SB1 candidates and all apart from #135 have been further investigated by Villaseñor et al. (2021). For #135, Dunstall et al. (2015) considered two He I lines at 4026 and 4387 Å and their radial velocity estimates at a given epoch differed by 20–60 km s $^{-1}$, probably due to the very strong nebular emission for these lines. We have repeated their cross-correlation analysis but now for three weaker He I lines at 4009, 4121, and 4144 Å. Inspection of these features shows little nebular emission, whilst the profiles appear symmetric. We obtain a smaller range in radial velocity estimates between epochs of 45 km s $^{-1}$ with typical uncertainties of ± 15 km s $^{-1}$. As such these variations do not fulfil one of the criteria of Dunstall et al. (2015) for binarity, viz. that the range should be more than four times the estimated uncertainties. Hence this target has been removed from the SB1 candidates. The status of the other six SB1 candidates is discussed in Section 6.6.

3 PROJECTED ROTATIONAL VELOCITY ESTIMATES

3.1 Methodology

Most of our targets have published estimates for their projected rotational velocity, $v_e \sin i$ (Dufton et al. 2013). However, given the complexities of Be-type spectra, our approach has been to re-estimate these and also to attempt to obtain estimates for the targets which had not been previously considered. We have used a Fourier transform (FT) methodology (Carroll 1933; Simón-Díaz & Herrero 2007) to estimate the projected rotational velocities following the procedures described in Dufton et al. (2013). This approach has been widely used for early-type stars (see for example Dufton et al. 2006; Lefever, Puls & Aerts 2007; Markova & Puls 2008; Simón-Díaz et al. 2010, 2017; Fraser et al. 2010; Dufton et al. 2013; Simón-Díaz & Herrero 2014) and relies on the convolution theorem (Gray 2005), viz. that

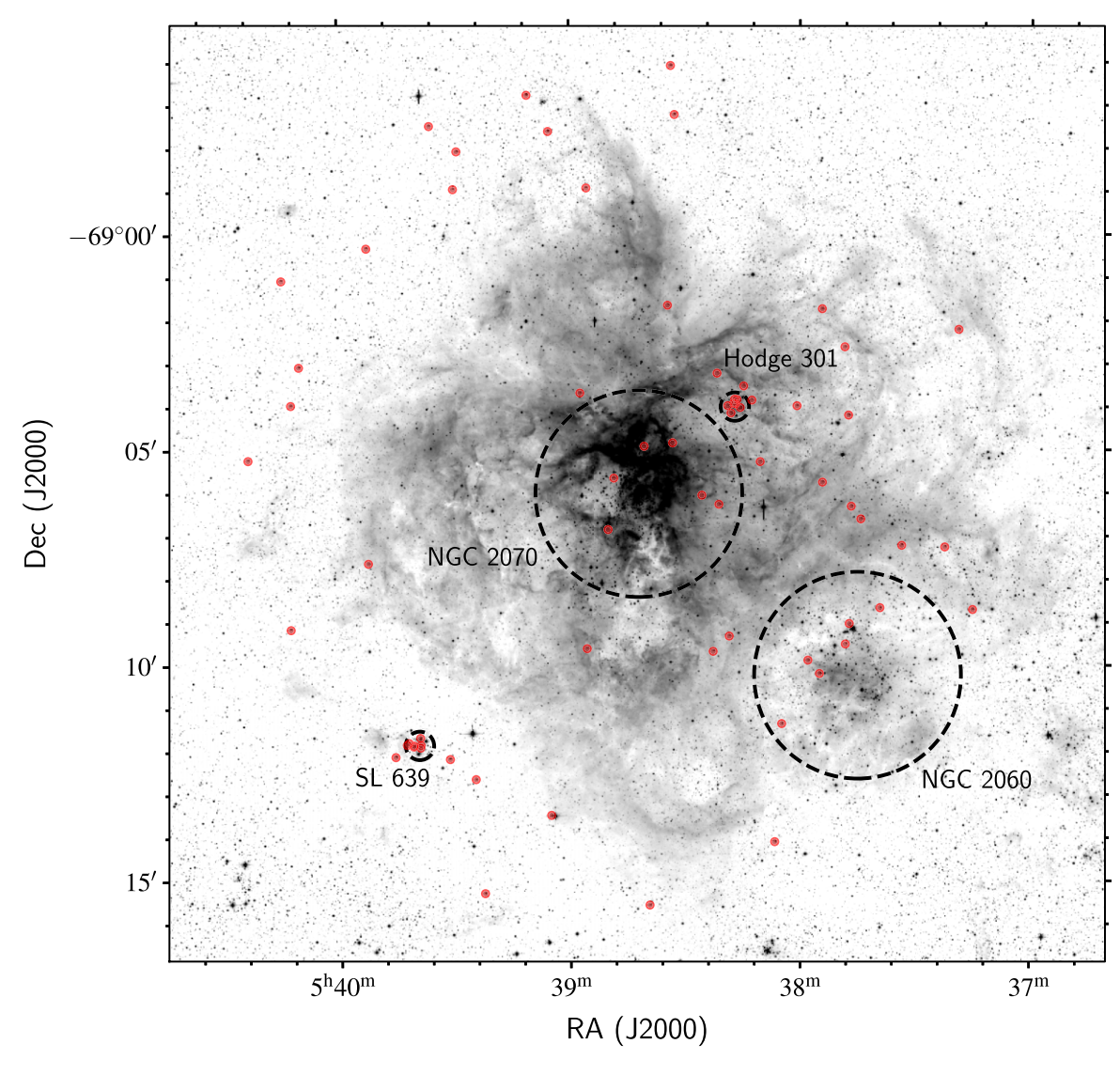


Figure 1. Spatial distribution of the Be-type targets in 30 Doradus. The spatial extents of NGC 2070, NGC 2060, SL 639, and Hodge 301 (Evans et al. 2015) are indicated by the overlaid dashed circles. The underlying image is from a V-band mosaic taken with the ESO Wide Field Imager on the 2.2-m telescope at La Silla.

the FT of convolved functions is proportional to the product of their individual FTs. It then identifies the first minimum in the FT for a spectral line, which is assumed to be the first zero in the FT of the rotational broadening profile with the other broadening mechanisms exhibiting either no minima or only minima at higher frequencies. Further details on the implementation of this methodology are given by Simón-Díaz & Herrero (2007) and Dufton et al. (2013).

As discussed by Simón-Díaz & Herrero (2007), the first minimum in the FT can be difficult to identify in spectra with, for example, low S/N or significant nebular contamination. Therefore we have also fitted rotational profiles to the observed spectral features. As we have not included either the intrinsic or instrumental broadening, the corresponding $v_e \sin i$ estimates may be overestimated, especially when the projected rotational velocity is relatively small – further details can be found in Dufton et al. (2013) and Ramírez-Agudelo et al. (2013, 2015). However these profile fitting (PF) estimates still provide a useful check on the FT estimates.

Two different sets of spectral lines have been adopted for analysis, depending on the degree of rotational broadening, and they are sum-

marized in Table 1. For the narrower-lined stars (with $v_e \sin i \lesssim 150 \, \mathrm{km \, s^{-1}}$), a selection of metal lines and non-diffuse helium lines was used. These have the advantage of being intrinsically narrow, whilst the former are not normally affected by nebula emission. For larger rotational velocities, reliable results could only be obtained from the stronger absorption lines and in these cases a selection of diffuse and non-diffuse helium lines was considered. Some features are close doublets or triplets, whilst additionally the He I diffuse lines have weak forbidden components in their blue wing. For the former, the separations were less than the broadening due to rotation and indeed the instrumental profile, whilst the latter were only used for the more rapidly rotating stars where the profiles appeared symmetric within the observational uncertainties.

Of the 73 VFTS Be-type targets (Evans et al. 2015), previous projected rotational velocities were available for 64 (Dufton et al.

¹For the spectral types considered here, blending of the He I line at 4026Å with a He II line should be unimportant.

3334 *P. L. Dufton et al.*

Table 1. Absorption lines (and their approximate wavelength in Å) that were used in estimating the projected rotational velocity. Possible blends are noted and for the He I features, those particularly prone to contamination by nebular emission are identified.

Species	λ	Set	Comment
Не і	4009	2	
Не і	4026	2	Nebular emission
Не і	4121	1,2	O II line at 4419Å
Не і	4144	2	
Не і	4169	1	
Сп	4267	1	
Не і	4387	2	
Не і	4471	2	Nebular emission
Mg II	4481	1	Al III line at 4479Å
Si III	4553	1	
Si III	4568	1	
Не і	4713	1,2	
Не і	4922	2	

2013; Garland et al. 2017). New estimates have been obtained here for all these targets plus five additional targets (#022, #030, #272, #293, and #395). The spectroscopy of the remaining four targets was not analysed as discussed in the supplementary material in Appendix A.

We have assigned a quality flag, Q, to our estimates for each target as specified below:

<u>Class 1</u>: Well observed He I or metal line spectrum with estimates being obtained from most lines. Features have a bell-shaped profile (supplemented by more extended wings for diffuse He I transitions, which exhibit linear Stark effect broadening), which are well fitted by a rotationally broadened profile with the appropriate $v_e \sin i$ -estimate. Little or no evidence for shell-like absorption or emission features. Some profiles may be affected by narrow emission (or absorption) features due to uncertainties in the removal of the nebular emission.

<u>Class 2:</u> As for Class 1 but the intrinsic weakness of the spectral features (often coupled with a moderate S/N) limits the number and accuracy of the $v_e \sin i$ -estimates. Additionally some He I lines (normally triplets) may show significant nebular contamination.

<u>Class 3:</u> Problematic spectra discussed in the supplementary material in Appendix A.

Means of the $v_e \sin i$ FT estimates for each star have been calculated by weighting individual estimates by the central depth of the line, to approximately allow for the differences in the observational quality. Unweighted means showed no systematic offset and agreed to typically 3 km s⁻¹ with a maximum difference of 10 km s⁻¹. Table 2 summarizes weighted means, their standard deviations, the number of lines considered, and their quality rating, Q. Also listed are spectral types (Evans et al. 2015), vesin i-estimates from the PF methodology, and signal-to-noise ratios (S/N). The last have been estimated for the wavelength region, 4200-4250 Å, which should not contain strong absorption lines. However particularly for the higher estimates, these should be considered as lower limits as they could be affected by weak features. S/Ns for the LR03 region were normally similar or slightly smaller (see for example, McEvoy et al. 2015, for a comparison of the ratios in the two spectral region).

The fits for the Class 1 objects were generally convincing and the means of the $v_{\rm e}\sin i$ -estimates were normally based on at least six independent measurements. Exceptions were #233 and #876 where only five estimates were available due to a relative low S/N in the LR03 spectroscopy and #874 where again five estimates were

available due to the metal line spectrum being relatively weak. However, the fits for these three targets appear reasonable whilst the standard deviation of the individual estimates are consistent with those for other targets with the highest quality rating.

For most of the Class 2 objects, the agreement between observation and the theoretical profiles was also reasonable, although now the number of estimates was generally smaller and/or nebular emission was present in some lines. In Appendix A (available as supplementary material), we comment on two Class 2 targets where the spectra presented additional problems. The estimates for the 14 targets with the lowest quality rating were affected by a variety of problems including strong nebular emission, low S/N spectroscopy, and close companions, and are all discussed in Appendix A.

In Appendix B (available as supplementary material), we discuss the stochastic uncertainties in the $v_{\rm e} \sin i$ -estimates, including those obtained from the different methodologies and different line-sets. We also compare our estimates with those obtained previously and conclude that a typical stochastic uncertainty would be 3–4 per cent, apart from the targets with Q = 3, where it would be larger.

3.2 Systematic errors in $v_e \sin i$ -estimates

For rapidly rotating stars, it is also important to consider systematic biases in the $v_e \sin i$ -estimates (Townsend, Owocki & Howarth 2004; Cranmer 2005; Frémat et al. 2005; Zorec et al. 2016). Their magnitude will depend on the stellar parameters some of which (for example, the angular velocity) may be unknown. Our approach has been to try to identify the largest plausible corrections, thereby estimating upper limits for the $v_e \sin i$ -distribution and in turn for the rotational velocity distribution.

The effects of stellar rotation on early-type stellar spectra have been investigated for over 40 yr (see for example, Collins & Sonneborn 1977; Collins, Truax & Cranmer 1991; Takeda, Kawanomoto & Ohishi 2017; Abdul-Masih et al. 2020, and references therein). Here, we utilize the simulations of Townsend et al. (2004) and Frémat et al. (2005) for B-type stars, including the early to mid-B-type stars, present in our samples. Townsend et al. (2004) considered spectral types between B0 and B9 and discussed possible biases for two lines considered here (He I 4471 Å and Mg II 4481 Å). The $v_e \sin i$ -underestimation was largest for targets at a near critical rotational velocity and observed at an angle of inclination, i $\sim 90^{\circ}$. Our targets have spectral types in the range B0–B3. For the former, they found underestimates of up to 12 per cent (He I 4471Å) and 9 per cent (Mg II 4481Å), increasing to up to 22 per cent and 12 per cent, respectively, for the B3 spectral type. To estimate the biases in our results, we have considered a spectral type B2 and used their results for the He I line as this ion was used for the broader lined targets and had the larger corrections. From their simulations, we can find the maximum correction as a function of the ratio of the measured $v_{\rm e}\sin i$ to the critical velocity ($v_{\rm crit}$). This correction was negligible for ratios of less than one half, increasing to reach more than 20 per cent at critical rotation.

Frémat et al. (2005) considered the same two lines and provided corrections for three effective temperatures (15 000, 20 000, and 24 000 K) and three gravities (3.4, 3.8, and 4.2 dex). In agreement with Townsend et al. (2004), they found that these were larger for helium than for magnesium, that they were anticorrelated with effective temperature, and that they fell very rapidly with decreasing angular velocity. We have adopted their corrections for $T_{\rm eff} = 24\,000$ K, and $\log g = 3.8$ dex in good agreement with the median atmospheric parameters of our data set (see Section 5). Additionally in order to estimate the maximum corrections, we used their simulations for an

Table 2. Estimates of the projected rotational and radial velocities. For the former, $v_e \sin i$ is the weighted mean of the FT estimates, σ the standard deviation, n the number of estimates, Q the quality estimate, whilst PF is the mean of the profile-fitting estimates. Also listed are estimates of the upper limits of the projected rotational velocity ($v_e \sin i_F$) after applying the corrections discussed in Section 3.2. Spectral types and sub-cluster membership (H: Hodge 301, S: SLS 639) are taken from Evans et al. (2015), whilst systems identified as SB1 binaries by Dunstall et al. (2015) and Villaseñor et al. (2021) are marked by asterisks. As discussed by Evans et al. (2006), the 'Be +' classification is on based on the identification of Fe II emission features. The full table is available as supplementary material.

VFTS	Spectral type	Cluster	S/N		Projected rotational velocity					Radial v	elocity	
				Set	$v_{\rm e} \sin i$	σ	n	Q	PF	$v_{\rm e} \sin i_{\rm F}$	$v_{\rm r}$	σ
022	B0-0.5 V-IIIe	_	65	2	364	36	4	3	312	406	262	26
030	B3-5e (shell)	_	65	2	295	20	4	2	309	317	263	17
034	B1.5 Ve	_	105	2	174	15	8	1	199	190	306	20
068	B1-1.5e	_	55	2	337	66	3	3	348	370	263	26
101	B0.7: Vne	_	95	2	358	19	7	1	342	398	273	21

angular velocity 99 per cent of critical. For both sets of corrections, we fitted a cubic polynomials with the appropriate independent variable: apparent $v_e \sin i$ for Frémat et al. (2005) and the ratio of the apparent $v_e \sin i$ to the critical velocity for Townsend et al. (2004). Corrections derived from these formulae agreed to typically $\pm 1 \,\mathrm{km}\,\mathrm{s}^{-1}$ with the original values.

For our sample, the correction deduced from the two sets of simulations² were qualitatively similar but those from Frémat et al. (2005) were systematically larger. For example, the mean difference in the corrections was 13 km s^{-1} , whilst that for the top quartile of $v_e \sin i$ -estimates was 16 km s^{-1} . These differences are not surprising as the corrections are based on different assumptions. In particular those of Frémat et al. (2005) can be considered as upper limits as we have assumed that all targets are rotating at effectively the critical velocity. In Table 2, projected rotational velocity estimates ($v_e \sin i_F$) including these corrections are listed and will be discussed in Section 6.

4 RADIAL VELOCITY ESTIMATES

Mean stellar radial velocity estimates have previously been estimated by Evans et al. (2015) for most of our targets. They were based on fitting Gaussian profiles to observed He I and/or metal lines. Given their relatively large projected rotational velocity, we have re-determined radial velocities for all the 63 targets which were not identified as SB1 systems. We utilized the central wavelengths found from profile fitting as discussed in Section 3, thereby limiting our estimates to those lines that had been used to estimate projected rotational velocities.

Initially we adopted laboratory wavelengths taken from the NIST Atomic Spectra Database (Kramida et al. 2018). However, all the diffuse helium lines contain a forbidden (P-F) component in their blue wing, together with other smaller asymmetries (Griem 1997). Evidence for this was found in the systematic offsets between the radial velocity estimates from different He I lines. In particularly the largest negative offsets were found for the diffuse triplet (at 4026 and 4471 Å), where the forbidden components are strongest.

We have therefore undertaken simulations to quantify the effects of these asymmetries for line-set 2 (see Table 1); no simulations were undertaken for line-set 1 as these should be symmetric. Three effective temperatures (20000, 23000, and 27500 K) and three gravities (3.0, 3.5, and 4.0 dex) were considered leading to a total of

nine combinations. This grid covered the estimated atmospheric parameters of over 80 per cent of the sample, with the remainder lying close to its edges. For each set of atmospheric parameters, helium line profiles were taken from the models discussed in Section 5 and convolved with a rotational broadening function for $v_e \sin i$ -values of 175, 275, and 400 km s⁻¹. Each profile was then fitted with a rotational broadening profile following the procedure used when analysing the observational spectroscopy. For each line and choice of $v_e \sin i$, we calculated the mean of the nine central wavelength estimates and their standard deviations. These are summarized in Table 3 together with the means and standard deviations averaged over all the simulations for a given line. For the non-diffuse (4121 and 4713 Å) and the singlet diffuse (4009, 4143, 4387, and 4921 Å) features, the mean wavelengths are in excellent agreement with the laboratory values. This is consistent with these features having theoretical profiles with a high degree of symmetry. By contrast the simulations for the two diffuse triplets (4026 and 4471 Å) give central wavelengths that are smaller by $\sim 0.2-0.3$ Å than the laboratory wavelengths of the allowed components. These shifts would be consistent with the observational offsets found from these lines when adopting laboratory wavelengths (see supplementary material in Appendix C).

Adopting the wavelengths implied by the simulations (last column of Table 3), we summarize the mean radial velocity estimates and their sample standard deviations in Table 2. These uncertainties are discussed in Appendix C (available as supplementary material), whilst estimates have not been undertaken for the targets classified as SB1 in Section 2. The same features were used as in the projected rotational velocity estimation and therefore the number of radial velocity estimates is again given by the values of n listed in Table 2.

5 STELLAR PARAMETERS

Effective temperatures, $T_{\rm eff}$, and logarithmic surface gravities, $\log g$ (in cm s⁻²) have been estimated for all our targets. The nature of Be-stellar spectra makes these parameters more difficult to estimate than for normal B-type stars (see for example, Dunstall et al. 2011; Ahmed & Sigut 2017). Indeed at near critical rotational velocities, the conventional model atmosphere assumption of plane-parallel (or spherical) geometry breaks down. Then as discussed by, for example, Zorec et al. (2016), these atmospheric parameters represent some average over the spatially varying photospheric conditions. Additionally the observed spectrum may be contaminated by emission from a circumstellar disc (Dunstall et al. 2011; Rivinius et al. 2013). Therefore, we have adopted a relatively simple approach, estimating $T_{\rm eff}$ from the spectral type and then the gravity from the higher-order

²Those for Townsend et al. (2004) used the critical velocities in Table 4

3336 *P. L. Dufton et al.*

Table 3. Laboratory and simulated wavelength for the He I lines used in the estimation of the radial velocity.

Line	Laboratory		Projected rotational velocity		All
	•	$175\;\mathrm{km}\mathrm{s}^{-1}$	$275 \; \text{km} \text{s}^{-1}$	$275 \; \mathrm{km} \mathrm{s}^{-1}$	
4009	4009.26	4009.24 ± 0.02	4009.28 ± 0.01	4009.21 ± 0.04	4009.24 ± 0.04
4026	4026.20	4026.07 ± 0.02	4026.10 ± 0.02	4026.06 ± 0.01	4026.08 ± 0.03
	4026.36				
4121	4120.82	4120.93 ± 0.03	4120.86 ± 0.02	4120.89 ± 0.06	4120.89 ± 0.05
	4120.99				
4144	4143.76	4143.81 ± 0.01	4143.82 ± 0.01	4143.82 ± 0.02	4143.82 ± 0.02
4388	4387.93	4387.93 ± 0.02	4387.96 ± 0.02	4388.01 ± 0.05	4387.97 ± 0.05
4471	4471.48	4471.34 ± 0.09	4471.30 ± 0.10	4471.27 ± 0.11	4471.30 ± 0.10
	4471.68				
4713	4713.16	4713.20 ± 0.06	4713.38 ± 0.06	4713.19 ± 0.02	4713.26 ± 0.10
	4713.38				
4922	4921.93	4921.90 ± 0.18	4921.94 ± 0.15	4921.90 ± 0.12	4921.92 ± 0.15

Table 4. Estimates of the atmospheric parameters, critical velocities (v_c) , and masses. Effective temperature estimates followed by a colon (:) assume a luminosity class V. The full table is available as supplementary material.

VFTS	$T_{ m eff}$	$\log g$	$v_{\rm c}$	$M\!/M_{\odot}$
022	29 600	3.60	471	21
030	19 000:	2.75	278	18
034	25 700:	4.30	585	10
068	26 200:	3.40	409	19
101	27 950	3.95	520	14

Balmer lines. In turn these have been used to estimate current stellar masses. Further details can be found as supplementary material in Appendix D and in Table 4.

These stellar parameters can also be used to estimate the stellar critical velocities and again details are provided as supplementary material in Appendix D, where we define three quantities following the nomenclature of Rivinius et al. (2013). Two of these, $v_{\rm orb}$ and $v_{\rm crit}$ are theoretical quantities with the former being the Keplerian circular orbital velocity and the latter this quantity for a star rotating at critical rotation. The third quantity, $v_{\rm c}$, is observational, being deduced from our estimated stellar parameters. Further details are provided in Appendix D and as discussed there,

$$v_{\text{orb}} \ge v_{\text{crit}} \ge v_{\text{c}}.$$
 (1)

Hence v_c estimates (which are listed in Table 4) will provide lower limits to either the critical, v_{crit} , or the orbital velocities, v_{orb} .

6 DISCUSSION

Below, we compare our estimates of Be-type stellar parameters with those obtained using similar methodologies (Dufton et al. 2013; Evans et al. 2015; Garland et al. 2017, and references therein) for other VFTS B-type stars, excluding supergiants and SB2 systems. We also consider equivalent samples of Be-type and B-type stars (again excluding supergiants and SB2 systems) towards the SMC young cluster, NGC 346. Stellar parameters have been estimated for these targets by Dufton et al. (2019), using similar methods to those adopted here. However the $v_{\rm e} \sin i$ -estimates were based on a single feature (either He I 4026Å or Si III 4553Å) and hence will be less reliable than those for the VFTS samples. Therefore, we have based our discussion principally on the VFTS samples and have mainly used the NGC 346 samples to check for consistency.

6.1 Projected rotational velocities

Table 5 summarizes statistics for $v_e \sin i$ -estimates of the Be- and B-type targets in the VFTS and NGC 346 surveys. The SB1 candidates and those showing no significant radial-velocity variations (henceforth designated as 'single-star') are considered separately.³ The Be-type single-star samples have medians (and means) between 240–270 km s⁻¹. Correcting the $v_e \sin i$ -estimates for possible systematic errors as discussed in Section 3.2 would increase these medians by typically 20 km s⁻¹. Similar statistics for the corresponding B-type stars are also summarized in Table 5 using the estimates in Dufton et al. (2013, 2019). Their medians and means are lower by typically 100 km s^{-1} than the comparable values for the Be-type samples.

Means for the Be-type SB1 candidates are also lower but are based on small sample sizes. Additionally comparisons of the estimates for single-star and SB1 samples are complicated by the possibility that the latter may be biased to systems with large orbital angles of inclination as discussed by Ramírez-Agudelo et al. (2015). However this would be expected to lead to an overestimation of the mean $v_e \sin i$ -estimate for the binary sample, whilst in fact the opposite is found

Recently several binary systems have been identified with Be-type characteristics and a very narrow lined primary spectrum, implying a projected rotational velocity of \lesssim 20 km s⁻¹. These include LB1 (Liu et al. 2019; Shenar et al. 2020; Simón-Díaz et al. 2020), HR 6819 (Bodensteiner et al. 2020b; Rivinius et al. 2020; El-Badry & Quataert 2021), and NGC 2004-115 (Lennon et al. 2021). The nature of these systems remains unclear, although it is unlikely that the primary is a typical Be-type star. All the SB1 systems in both of our samples have significantly larger $v_e \sin i$ -estimates (see Table 2) and are hence unlikely to be analogs of these systems.

In Fig. 2, cumulative distribution functions (CDFs) are shown for our apparently single B-type and Be-type stellar samples. The apparent difference between the CDFs for our two B-type samples has been discussed by Dufton et al. (2019). They suggested that it might reflect the larger number of cluster members in the VFTS sample, although the differences were found to be not statistically significant at a 5 per cent threshold. Also shown in In Fig. 2 is the CDF for the sample of Galactic Be-type stars discussed by Zorec et al. (2016).

All the single Be-type single-star samples have a similar distributions, although there is evidence of more targets with lower

³The single-star samples are likely to contain unidentified binaries as discussed by Dunstall et al. (2015)

Table 5. Median and means for the $v_e \sin i$ -estimates for the non-supergiant targets in the VFTS and NGC 346 surveys. Statistics are given for subgroups with different spectral classifications.

Data set	S	Sample		sured	Fré	mat		
		_	Median	Mean	Median	Mean	n	
VFTS	Be-type	Single	268	257	287	282	63	
VFTS	B-type	Single	173	173	189	191	219	
VFTS	Be-type	SB1	219	218	237	243	6	
VFTS	B-type	SB1	129	138	145	153	91	
NGC 346	Be-type	Single	242	245	259	270	62	
NGC 346	B-type	Single	113	125	129	137	158	
NGC 346	Be-type	SB1	229	205	246	222	4	
NGC 346	B-type	SB1	137	141	153	155	29	

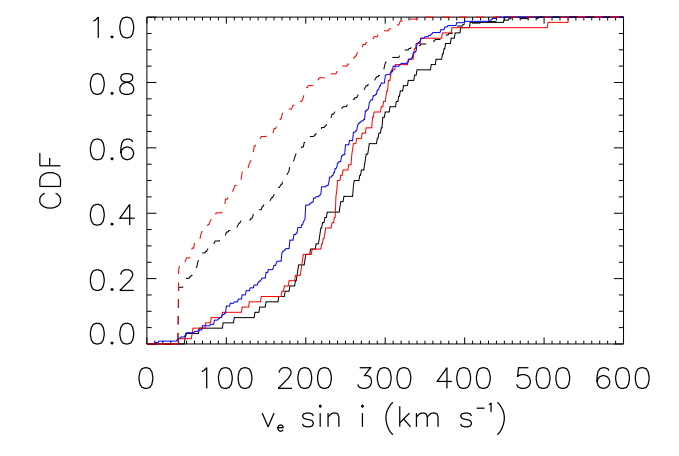


Figure 2. Cumulative distribution function for the VFTS (black lines) and NGC 346 (red lines) $v_e \sin i$ -estimates. Solid lines are for the apparently single Be-type samples and dashed lines for the corresponding samples of non-supergiant B-type stars. Also shown is the cumulative distribution function for the Galactic Be-type sample of Zorec et al. (2016) (blue solid line).

 $v_{\rm e}\sin i$ -estimates in the Galactic sample. However Kolmogorov–Smirnov (KS) tests (Fasano & Franceschini 1987) implied that these differences were not significant at the 10 per cent level, whilst the selection criteria for the three samples are different. Hence we conclude that there is no significant evidence of rotational velocity differences between the Galactic and Magellanic Cloud Be-type samples.

A KS test returned very small probabilities ($<10^{-4}$ per cent) that our single Be-type and corresponding B-type subgroups are from the same parent population for both the VFTS and the NGC 346 samples. For the SB1 Be-type systems, KS tests found no statistical significant differences at the 10 per cent level between either the Be-type stars from the two surveys or between the Be-type samples and their corresponding B-type sample. This is consistent with the small number of SB1 systems in both surveys.

In summary, the means and medians of the $v_{\rm e} \sin i$ -estimates for Betype stars in both surveys are larger by typically 100 km s⁻¹ higher than those for the corresponding B-type stellar samples. In turn statistical tests imply a very small probability of them having arisen from the same parent population.

6.2 Rotation at near critical velocities

Our Be-type samples appear to be rotating at systematically larger velocities than the corresponding B-type samples as has been found

Table 6. Monte Carlo simulations for the number $(N_{\rm crit})$ of VFTS Betype stars that would have a projected rotational velocity $(v_{\rm e}\sin i)$ less than some fraction $(F_{\rm crit})$ of the critical velocity $(v_{\rm crit})$. The simulations assume a Gaussian distribution of equatorial rotation velocities (see equation 2) with a $\sigma=0.02$ and centred at $\gamma_{\rm cent}$ of 0.7, 0.8 and 0.9.

γcent		$F_{ m crit}$						
	0.5	0.4	0.3	0.2				
Obs	23	13	7	5				
Scaled	20	11	6	3				
0.7	20.8 ± 3.8	12.4 ± 3.2	6.7 ± 2.5	2.9 ± 1.7				
0.8	15.2 ± 3.4	9.3 ± 2.8	5.1 ± 2.2	2.2 ± 1.5				
0.9	11.6 ± 3.1	7.2 ± 2.6	4.0 ± 2.0	1.7 ± 1.3				

in many previous studies (see for example, Struve 1931; Cranmer 2005; Frémat et al. 2005; Dunstall et al. 2011; Rivinius et al. 2013; Zorec et al. 2016). Indeed it is often assumed that all Be-type stars are rotating at near critical velocities (see for example, Rivinius et al. 2013; Bastian et al. 2017). To test this assumption for our Be-type samples, we have undertaken Monte Carlo simulations for a Gaussian distribution of rotational velocities,

$$p(\gamma_{\rm e}) = \frac{1}{\sigma\sqrt{2\pi}} \exp\left(\frac{(\gamma_{\rm e} - \gamma_{\rm cent})^2}{2\sigma^2}\right),\tag{2}$$

where γ_e is the equatorial rotational velocity in units of the critical velocity,

$$\gamma_{\rm e} = \frac{v_{\rm e}}{v_{\rm crit}},\tag{3}$$

We have adopted $\sigma = 0.02$ and three values of $\gamma_{\rm cent}$, viz 0.7, 0.8, and 0.9 and then simulated the corresponding $v_{\rm e}\sin i$ -distributions assuming that $\sin i$ is randomly distributed. Scaling by the VFTS sample size, leads to estimates of the number of targets ($N_{\rm crit}$) with projected rotational velocities less than some fraction ($F_{\rm crit}$) of the critical velocity,

$$F_{\rm crit} = \frac{v_{\rm e} \sin i}{v_{\rm crit}}.\tag{4}$$

Table 6 summarizes the predicted means (and standard deviations) of $N_{\rm crit}$ for upper limits of $F_{\rm crit}$ ranging from 0.5 down to 0.2. Also listed are the observed numbers of VFTS targets using both the measured and the scaled $v_{\rm e}{\sin i}$ -estimates listed in Table 2. Reasonable agreement with observation is found for $\gamma_{\rm cent}{\sim}0.7$. By contrast, all of the observed values are larger than predicted when $\gamma_{\rm cent}{\geq}0.8$.

To investigate this further, we have also used our Monte Carlo simulations to estimate the likelihood that the observed $N_{\rm crit}$ values

Table 7. Monte Carlo simulations of the percentage probability of obtaining the observed number $(N_{\rm crit})$ of Be-type stars that have a projected rotational velocity $(v_{\rm esin}\,i)$ less than some fraction, $F_{\rm crit}$, of the critical velocity, $v_{\rm crit}$. The simulations assume Gaussian distribution of equatorial rotation velocities with a σ of 0.02 and centred at $\gamma_{\rm cent}$ of 0.7, 0.8, and 0.9. Also listed are the centres that best reproduce the $N_{\rm crit}$ values (designated 'Implied'). Both sets of $N_{\rm crit}$ estimates listed in Table 6 have been considered.

$v_{\rm e} \sin i$	Centre		F_{ϵ}	crit	
scaled	$\gamma_{ m cent}$	0.5	0.4	0.3	0.2
No	0.9	<0.1 per cent	2.6 per cent	10.3 per cent	3.1 per cent
	0.8	2.0 per cent	13.1 per cent	24.5 per cent	7.1 per cent
	0.7	32.4 per cent	47.6 per cent	50.9 per cent	16.8 per cent
Implied γ_{cent}		0.67	0.69	0.69	0.54
Yes	0.9	0.9 per cent	10.5 per cent	20.8 per cent	25.2 per cent
	0.8	10.7 per cent	32.2 per cent	39.6 per cent	38.2 per cent
	0.7	63.1 per cent	71.8 per cent	67.0 per cent	55.6 per cent
Implied γ_{cent}		0.71	0.74	0.74	0.69

(or larger) would be observed and summarize the results in Table 7. For both sets of $v_{\rm e}{\rm sin}\,i$ -estimates, $\gamma_{\rm cent}=0.9$ is inconsistent with the observations at a 5 per cent threshold, whilst adopting $\gamma_{\rm cent}=0.8$ leads to percentages that are still relatively low. By contrast a value of $\gamma_{\rm cent}=0.7$ leads to relatively high levels of likelihood, consistent with the predicted and observed $N_{\rm crit}$ values being in good agreement.

This comparison implies that not all our targets can be rotating at near critical equatorial rotational velocities. Both Townsend et al. (2004) and Frémat et al. (2005) found that the $v_e \sin i$ -corrections decreased rapidly with decreasing γ_e . For example, Frémat et al. (2005) found a typical correction of $10 \, \mathrm{km \, s^{-1}}$ for a B2 V star rotating with $\gamma_e = 0.8$. Hence adopting the measured $v_e \sin i$ -estimates for N_{crit} may provide a more realistic comparison. Now the simulations with $\gamma_{cent} \geq 0.8$ are also inconsistent with the observations at a 5 per cent likelihood threshold.

An equivalent comparison for the NGC 346 sample led to similar results. The simulations for $\gamma_{\rm cent} \ge 0.8$ are now inconsistent with all the observed $N_{\rm crit}$ -estimates at a 5 per cent likelihood threshold, with again reasonable agreement being found for $\gamma_{\rm cent} \sim 0.7$

We have used our Monte Carlo simulations to estimate the γ_{cent} values which lead to predicted mean numbers of VFTS targets being identical to those observed. These are summarized in Table 7 (designated as 'Implied') and lead to γ_{cent} values of \sim 0.7; similar values were found for the NGC 346 sample.

The simulations have been repeated with σ increased to 0.05. Estimated means and standard deviations of the $N_{\rm crit}$ values were both increased by typically 1–2 per cent, whilst the implied values of $\gamma_{\rm cent}$ were effectively unchanged. We have not considered further increases as this would be lead to significant numbers of targets that do not rotate at near critical velocities, inconsistent with the assumption that we were testing.

To investigate the sensitivity of our results to the distribution of rotational velocities, we have also considered a step function, as follows:

$$p(\gamma_{\rm e}) = \frac{1}{1 - \gamma_{\rm m}} \text{ for } 1 \ge \gamma_{\rm e} \ge \gamma_{\rm m}$$

$$= 0 \text{ otherwise.}$$
 (5)

Monte Carlo simulations were performed for γ_m -values of 0.7, 0.8, 0.9, and the results are summarized in Table 8. The simulations are qualitatively similar to those found adopting a Gaussian distribution, with all of them being inconsistent with the observations at a 5 per cent statistical level. Additionally the γ_m -values required to match the observed values are \sim 0.5. The implication of these sim-

ulations is that any $p(\gamma_e)$ -distribution that agreed with the observed F_{crit} -values would have to extend to relatively low γ_e -values.

In summary, the MC simulations are inconsistent with all Betype stars in our two samples rotating at near critical velocities. Adopting a Gaussian distribution for γ_e implies $\gamma_{cent} \sim 0.65-0.75$, in good agreement with the mode of the γ_e -distribution found by Zorec et al. (2016) for a sample of Galactic Be-type stars – this will be discussed further in Section 6.4

6.3 Rotational velocity distributions, v_e

Our sample of single VFTS Be-type contains only 63 targets but can be used to constrain the current distribution of their equatorial rotational velocities. Assuming that their rotation axes are randomly distributed, we can infer the normalized probability density function distribution, $p(v_e)$, using the iterative procedure of Lucy (1974) as implemented by Dufton et al. (2013), where further details can be found. In Fig. 3, these are shown for both the measured and scaled $v_e \sin i$ -estimates; tests showed that including the six SB1 systems did not significantly alter these distributions. Distributions for the single B-type VFTS sample, discussed in Section 6.1 are also shown in Fig. 3.

Given the relatively small size of the Be-type sample, care should be taken in interpreting these results. In particular, structure with a velocity scale similar to the binning interval of 40 km s⁻¹ used for the observational estimates may not be real. However, there does not appear to be a significant number of Be-type stars with equatorial velocities, $v_e \lesssim 150 \text{ km s}^{-1}$. Additionally the maximum equatorial rotational velocity would appear to be in the range $\sim 550-600 \text{ km s}^{-1}$. In Table 9, we list the median and means for different probability distributions. For the Be-type stars they are in the range 320–350 km s⁻¹, compared with 220–250 km s⁻¹ for the other B-type stars, consistent with the $v_e \sin i$ -statistics in Table 5 after scaling by the mean value of $\sin i = \pi/4$ (Gray 2005).

Equatorial velocity distributions have also been inferred using the same methodology for the apparently single B-type and Betype stars towards NGC 346 (Dufton et al. 2019) and are shown in Fig. 4. The distribution for the measured $v_e \sin i$ -estimates show a small peak at $\sim 550 \text{ km s}^{-1}$, due to two fast rotating targets (#1134 and #1174) that may have unusual evolutionary histories (Dufton et al. 2019). Applying the corrections of Frémat et al. (2005) led to $v_e \sin i$ -estimates (>600 km s⁻¹), which were significant larger than the estimated critical velocities; they were therefore excluded from the de-convolution for the scaled estimates. Compared with the

Table 8. Monte Carlo simulations of the percentage probability of obtaining the observed number $(N_{\rm crit})$ of Be-type stars that have a projected rotational velocity $(v_{\rm e}\sin i)$ less than some fraction, $F_{\rm crit}$, of the critical velocity, $v_{\rm crit}$. The simulations assume a step function starting at $\gamma_{\rm m}$, with values of 0.7, 0.8, and 0.9 being considered. Also listed are the $\gamma_{\rm m}$ -values that best reproduce the $N_{\rm crit}$ values (designated 'Implied'). Both sets of $N_{\rm crit}$ estimates listed in Table 6 have been considered.

$v_{\rm e} \sin i$	Step position		F_{c}	crit	
scaled	γm	0.5	0.4	0.3	0.2
No	0.9	<0.1 per cent	1.0 per cent	6.4 per cent	2.0 per cent
	0.8	<0.1 per cent	2.7 per cent	10.6 per cent	3.1 per cent
	0.7	0.5 per cent	7.4 per cent	18.6 per cent	5.0 per cent
Implied $\gamma_{\rm m}$		0.49	0.48	0.47	0.30
Yes	0.9	0.2 per cent	5.5 per cent	14.5 per cent	20.7 per cent
	0.8	1.0 per cent	10.7 per cent	21.1 per cent	25.7 per cent
	0.7	4.7 per cent	22.2 per cent	31.1 per cent	32.7 per cent
Implied γ_m		0.53	0.55	0.55	0.48

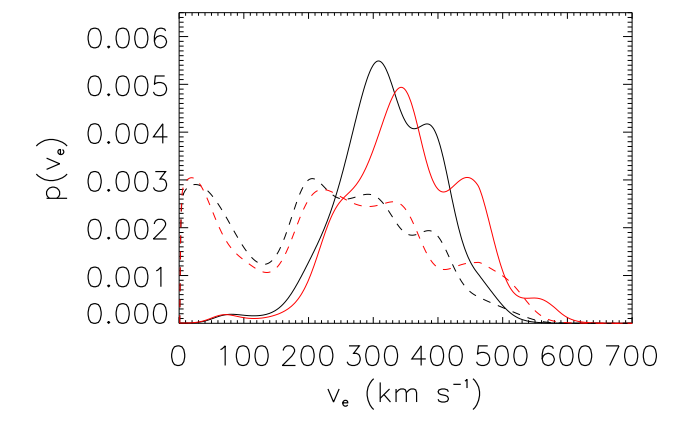


Figure 3. Rotational velocity distributions for apparently single VFTS targets. Black and red solid lines are for the Be-type subsample, with the latter including corrections estimated from Frémat et al. (2005). Dotted lines are analogous results for the B-type sample, excluding Be-type and supergiant targets.

Table 9. Median and means for the deconvolved rotational velocity distributions for the apparently single non-supergiant targets in the VFTS and NGC 346 surveys. The columns labebelled 'Frémat' have used the $v_e \sin i_F$ -estimates listed in Table 2.

Data set	Sample	Meas	sured	Frémat	
		Median	Mean	Median	Mean
VFTS	Be-type	323	325	349	353
VFTS	B-type	226	223	246	243
NGC 346	Be-type	305	309	323	323
NGC 346	B-type	155	168	169	181

VFTS distributions, there again appears to be few (if any) slowly rotating Be-type stars, whilst the upper limit is similar (although possibly slightly lower). The corresponding means and medians for the NGC 346 samples are also listed in Table 9. The Be-type values are similar to those for the VFTS samples but those for the B-type sample are lower, as discussed in Section 6.1 for the $v_e \sin i$ -estimates.

In summary, both samples of Be-type stars show an absence of stars with $v_{\rm e} \lesssim 150~{\rm km~s^{-1}}$ and an upper limit for the equatorial velocity of 500–600 km s⁻¹. They have mean equatorial velocities in the range 310–350 km s⁻¹, whilst there is no convincing evidence for structure in their probability density function distribution, $p(v_{\rm e})$.

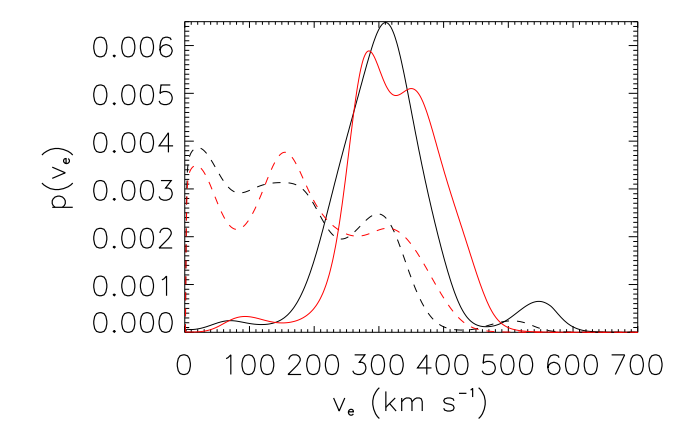


Figure 4. Rotational velocity distributions for apparently single NGC 346 targets. See the caption to Fig. 3 for further details.

6.4 γ_e -distributions, $p(\gamma_e)$

The normalized probability distribution, $p(\gamma_e)$, introduced in equation (2) can be inferred by deconvolving the $F_{\rm crit}$ values deduced from the $v_e \sin i$ and v_c estimates. The uncorrected estimates, listed in Tables 2 and 4, respectively, were initially adopted but we discuss this further below. The de-convolved probability distributions for the VFTS apparently single Be-type data set is shown in Fig. 5, together with that deduced for the NGC 346 sample. We have also performed similar de-convolutions for the corresponding B-type samples introduced in Section 6.1 and these are also shown in Fig. 5. The v_c -estimates utilized the stellar parameters in Schneider et al. (2018) for the VFTS sample and in Dufton et al. (2019) for the NGC 346 sample.

The two probability distributions for the Be-type samples have similar characteristics with a dearth of targets at $\gamma_e \lesssim 0.4$ and extending to $\gamma_e > 1$, which would imply equatorial rotational velocities in excess of the critical velocity. For the VFTS, this would constitute ~ 17 per cent of the Be-type sample, increasing to ~ 27 per cent after applying the $v_e \sin i$ -corrections of Frémat et al. (2005). The percentages for the NGC 346 sample would be 7 per cent and 14 per cent, respectively. By contrast the B-type samples have a significant number of targets at small γ_e -values, with <4 per cent of the VFTS sample and <1 per cent of the NGC 346 having $\gamma_e > 1$.

Zorec et al. (2016) undertook a similar de-convolution for Galactic Be-type stars and found approximately 4 per cent of their sample also had $\gamma_e > 1$. They considered the systematic biases on their $v_e \sin i$ and

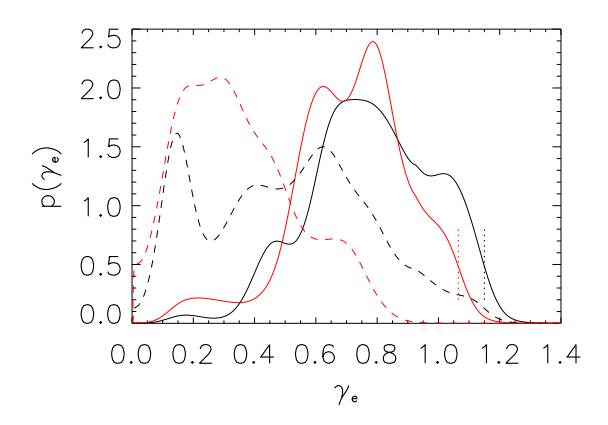


Figure 5. γ_e -distributions for apparently single Be-type targets. Black and red solid lines are for the the VFTS and NGC 346 samples respectively. Dotted lines show the adopted maximum values for the distributions as discussed in Section 6.4. Dashed lines are the distributions for the analagous B-type samples.

 $v_{\rm crit}$ estimates on a star-to-star basis and generally found that their $F_{\rm crit}$ estimates were reduced. These biases are the most likely explanation of the extension of our $\gamma_{\rm e}$ -distributions beyond $\gamma_{\rm e} > 1$.

We have attempted to estimate the overall effect of these biases by identifying upper limits, $\gamma_{\rm max}$ for the $\gamma_{\rm e}$ -distibutions. We have adopted a limit at which 98 per cent of the $\gamma_{\rm e}$ -distributions would have $\gamma_{\rm e} < \gamma_{\rm max}$. This leads to $\gamma_{\rm max}$ estimates of 1.150 and 1.064 for the VFTS and NGC 346 samples, respectively, and these are illustrated in Fig. 5. Scaling our distributions by these estimates would lead to median (and means) for both our data sets of \sim 0.68 in excellent agreement with the estimate of Zorec et al. (2016) of 0.64–0.68 for their Galactic sample. Our choice of $\gamma_{\rm max}$ is of course subjective but clearly some adjustment is required to ensure a physically realistic distribution. For the VFTS and NGC 346 B-type samples, the corresponding $\gamma_{\rm e}$ -medians would be \sim 0.51 and \sim 0.32, respectively, reflecting the lower estimates of the $v_{\rm e}$ -means of the latter shown in Table 9.

Recently Balona & Ozuyar (2020a, b) have discussed TESS photometry of over 400 Galactic Be-type stars. The majority are short term variables and their $v_e \sin i$ -estimates imply that their fundamental periods reflect rotational modulation. In turn these allow estimates of their equatorial velocities and hence of $p(\gamma_e)$ (see fig. 5 of Balona & Ozuyar 2020a), which is similar to that of Zorec et al. (2016) and to those shown in Fig. 5. For example, there is a lack of Be-type stars with $\gamma_e \lesssim 0.3$ and then a broad distribution up to $\gamma_e \sim 1$. For early Be-type stars, their mean γ_e -value is ~ 0.65 in excellent agreement with the values discussed above. However, although the methodology of Balona & Ozuyar (2020a, b) is independent of those used by Zorec et al. (2016) and here, it depends on an identified frequency being due to rotational modulation. As discussed by Labadie-Bartz et al. (2020) and Barraza et al. (2022), the frequency spectra of the TESS photometry for Be-type stars are complex and diverse with essentially all targets being variable over different time cadences. Additionally they identify several other mechanisms that may lead to variability besides rotational modulation.

In summary, the deconvolved γ_e -distributions for both Magellanic Cloud data sets are similar and imply a dearth of targets with $\gamma_e \lesssim 0.4$, with a broad distribution reaching up to critical rotation, $\gamma_e \simeq 1$. Our best estimate for the mean or median of the γ_e -distribution is ~ 0.68 . These characteristics are in agreement with those found by Zorec et al. (2016) and Balona & Ozuyar (2020a, b) for Galactic samples.

6.5 Rapidly rotating Be- and B-type stars

The v_e -distributions in Figs 3 and 4 imply that there are a significant number of apparently single rapidly rotating B-type stars that do not currently exhibit Be-type characteristics. We have estimated the relative numbers of rapidly rotating Be-type and B-type stars in our two samples using lower limits to the equatorial rotational velocity of 200 and 300 km s⁻¹. Essentially all (\sim 95 per cent) Betype stars were included using the former limit and between 50 and 70 per cent for the later. The percentages were lower for the Btype stars ranging from \sim 20 to 60 per cent. To estimate the actual number of targets, these percentages must be scaled by the number of targets and these estimates are summarized in Table 10. For both data sets, there are a significant number of rapidly rotating B-type stars, leading to a Be-type to B-type ratio (R) of $\sim 0.5-0.7$ for the VFTS sample and $R \sim 1.0-1.5$ for the NGC 346 sample. Apart from stochastic uncertainties, this variation in R could reflect intrinsic differences between the two samples that are discussed as supplementary material in Appendix E.

Using the inferred γ_e -distributions shown in Fig. 5, we can undertake a similar comparison in terms of γ_e . We have considered lower limits for γ_e of 0.6 and 0.8 and summarize the results in Table 10. For the VFTS sample, the number of B-type stars is similar to or greater than that for the Be-type stars, in agreement with the the comparison for the ν_e -distribution. By contrast, the Be-type stars are more numerous in the NGC 346, especially for the case with $\gamma_e \ge 0.8$. However it should be noted that this sample relates to only the \sim 30 per cent of the Be-type stars with the largest γ_e -values. Additionally we have not corrected the γ_e -distributions to account for the significant number of Be-type stars with $\gamma_e > 1$.

For the VFTS sample (which is better constrained in terms of target selection, environment, and binarity identification), the B-type stars are more prevalent than the Be-type stars, when considering either the $v_{\rm e}$ -distributions or the $\gamma_{\rm e}$ -distributions. This is consistent with the magnitude limited samples of Be-type and Bn-type stars drawn from the Bright Star Catalogue (Hoffleit & Jaschek 1991) and discussed by Rivinius et al. (2013). Given the transitory nature of the Be-type phenomena (see for example, Rivinius et al. 2013), some of the rapidly rotating B-type stars may be quiescent Be-type. Unfortunately, statistics for the duration of the Be-type and quiescent phases are not available and hence it is not possible to estimate the number of rapidly rotating B-type stars that are quiescent Be-type.

6.6 Binarity

Relatively few binary Be-type candidates have been identified in either the VFTS or NGC 346 data sets. This is consistent with a recent study of multiplicity in Galactic (Bodensteiner et al. 2020b) and SMC (Bodensteiner et al. 2021) Be-type samples. The latter utilized MUSE spectroscopy of the core of NGC 330 and found that the observed spectroscopic binary fraction of Be-type stars (2 \pm 2 per cent) was lower than that for B-type stars (9 \pm 2 per cent).

The time cadence of our NGC 346 observations was limited with between two and four epochs covering a period of 6 weeks or less. Additionally the adopted methodology (Dufton et al. 2019) would only have identified systems with relatively large radial velocity variations. Hence, here, we concentrate on the VFTS targets that typically had six epochs with the time cadence (Evans et al. 2011) such that the predicted detection probability for massive primaries having secondaries with a mass ratio, q > 0.1, was greater than 60 per cent for periods of \leq 100 d (Sana et al. 2013; Dunstall et al. 2015).

Table 10. Estimated numbers of Be-type and apparently single B-type stars with equatorial rotational velocities (v_e) greater than 200 or 300 km s⁻¹. Results are obtained using the probability distributions, $p(v_e)$ discussed in Section 6.3, scaled by the sample size, N. Comparable estimates are also provided for the number of targets with γ_e -values greater than 0.6 and 0.8, using the probability distributions, $p(\gamma_e)$ discussed in Section 6.4.

Data set Sample N		N	Measured		Frémat		γe	
			>200	>300	>200	>300	>0.6	>0.8
VFTS	Be-type	69	65	43	64	48	57	32
VFTS	B-type	219	126	66	127	80	86	32
NGC 346	Be-type	66	62	35	63	40	50	23
NGC 346	B-type	158	58	23	64	30	21	2

Table 11. Number of targets (n) and binary candidates (SB1) in the VFTS Be-type and B-type samples. Also listed are the p-statistic from χ^2 and Fischer statistical tests.

Line-set	Sample	n	SB1	$p(\chi^2)$	p(Fischer)
1	Be-type B-type	11 137	2 51	0.20	0.33
2	Be-type B-type	58 173	4 40	0.0065	0.0062
Both	Be-type B-type	69 310	6 91	0.0037	0.0028

The accuracy of the radial velocity estimates depended on, inter alia, the S/N of the spectroscopy, and the degree of rotational broadening. For the VFTS sample, the standard deviations for the radial velocity estimates for a given target and epoch covered a wide range from <1 to $\sim\!50~{\rm km\,s^{-1}}$ with a median of 6.8 km s $^{-1}$. The primary criterion for binarity was that variations in the radial velocity estimates were significant at a 4σ -level. Excluding supergiants, all identified B-type binaries had a range of radial velocity estimates, $\gtrsim\!20~{\rm km\,s^{-1}}$. For the VFTS Be-type sample, the median of the standard deviations for the radial velocity estimates for a given target and epoch is 11.0 km s $^{-1}$. The increase over that for the B-type sample reflects the greater rotational broadening in the Be-type sample.

The lower fraction of *detected* binary in the VFTS Be-type sample compared with that for the B-type sample could be due to real differences. Alternatively it could just reflect the intrinsic difficult of estimating radial velocities for Be-type stars, together with the relatively small sample size. To test the latter, we list in Table 11, the number of VFTS Be-type and B-type SB1 candidates using the different sets of lines summarized in Table 1. The Be-type statistics exclude the target #135 for the reasons discussed in Section 2.2; those for the B-type targets were taken from Dunstall et al. (2015) and assigned to the different line-sets using Dufton et al. (2013).

Only 11 Be-type stars were analysed using line-set 1 of which two are SB1 candidates, equating to \sim 20 per cent; for the 137 B-type targets, 51 stars were identified as SB1 candidates, corresponding to \sim 40 per cent. However as can be seen from Table 11 high probabilities are returned that these are from the same population using both a χ^2 or Fischer test (Miodrag 2011). For line-set 2, the sample sizes are larger and lead to observed binary fractions of \sim 7 per cent and 23 per cent for the Be-type and B-type samples, respectively. Now the statistical tests imply that the difference in the observed binary fraction is significant. For completeness, we have also considered the complete samples (both line-sets 1 and 2) and again the statistical tests imply that the binary fraction in the two samples differ.

The above analysis does not take into account the larger uncertainties in the Be-type radial velocity estimates. We have attempted to investigate this as follows. As discussed above, the threshold for identifying binaries was approximately three times the median uncertainty in the radial velocity estimates. Excluding B-type binaries with ranges in radial velocity estimates less than three times the median Be-type uncertainty would decrease the number of B-type binaries identified to 71. In turn this would lead to p-statistics of $0.036~(\chi^2)$ and 0.040~(Fischer). These are still both statistically significant at a 5 per cent level implying that the different binary fractions are not due to different observational uncertainties. We emphasize that this comparison is only relevant to differences in the binary populations for systems that would have been detectable for the VFTS sample. As discussed above this would be for massive binaries with periods, $P \lesssim 100~\text{d}$ and with mass ratios, $q \gtrsim 0.1$.

If the binary fraction of such Be-type stars was smaller than that of the normal B-type stars, then one consequence could be a smaller measured radial velocity dispersion for the Be-type stars. While the VFTS data are well suited to this task, the full B-type stellar sample in the 30 Dor region has a large velocity dispersion, $\sim\!20~{\rm km\,s^{-1}}$, and significant velocity structure, that could obscure any potential difference between Be-type and non-Be-type stars. However the VFTS survey region contains two older clusters, Hodge 301 and SL639, both of which have main sequence early B-type stars with well-defined cluster velocities. As the sample sizes for each cluster are small, we combine them after shifting their stellar radial velocities to the rest frame cluster velocities (Patrick et al. 2019), giving a total of 11 B-type stars, and 16 Be stars.

Normalized probability density plots are shown in Fig. 6 and hint at a smaller velocity dispersion for the Be-type stars, with weighted sample standard deviations of 8.3 km s⁻¹ for the B-type stars, but only 3.5 km s⁻¹ for the Be stars. The methodology for the B-type radial velocity estimates differed from that for the Be-type stars as it used Gaussians in the profile fitting and did not include systematic offsets in the He I lines discussed in Appendix C. For the former, targets with low $v_e \sin i$ -estimates that utilized line-set 1 yielded central wavelength that agreed to within 0.01Å irrespective of the adopted profile. Targets utilizing line-set 2 showed differences of typically 0.05 Å, equating to 3–4 km s⁻¹. However the variations were not systematic implying that the uncertainties in the mean radial velocity estimates would be smaller. The choice of either the laboratory wavelengths or those adopted here (see Table 3) typically changed the mean radial velocity estimates by 3-4 km s⁻¹ but as these changes were systematic the changes in the velocity dispersion would be smaller.

Given these uncertainties and the small sample sizes, the differences in the velocity dispersion from the two samples may not be significant. However they imply that there is a smaller SB1 Be-type fraction with orbital parameters similar to those of the B-type SB1

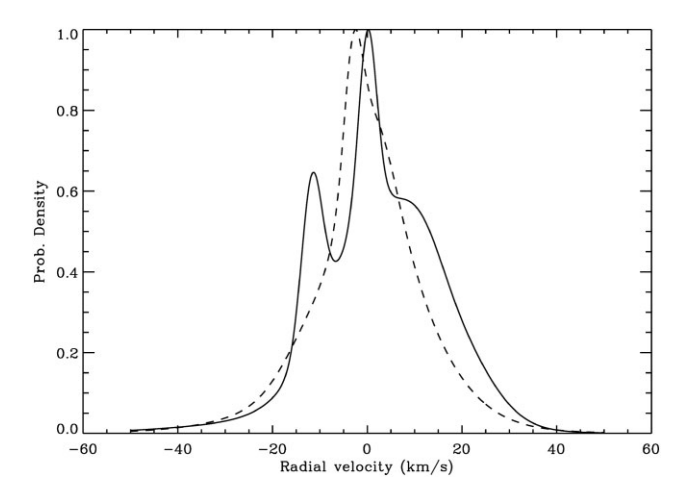


Figure 6. Combined probability densities for the radial velocity estimates of the Be-type (dotted line) and B-type (solid line) targets in Hodge 301 and SL639.

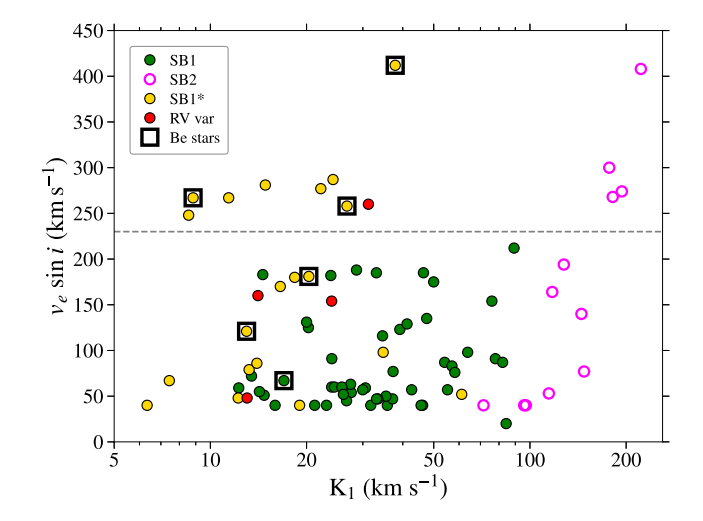


Figure 7. Estimated semi-amplitudes for VFTS binary candidates taken from Villaseñor et al. (2021) plotted against their estimated projected rotational velocities. Be-type stars are shown with black boxes.

population. This would be consistent with either Be-type stars being formed by a single star evolutionary channel or being the products of post-transfer (case-B) binaries. The latter has been discussed by Shao & Li (2014) and Langer et al. (2020), who predict periods of the order of a few 100 days to a few years. Such binaries would have be difficult to detect with the VFTS time cadence (Dunstall et al. 2015), especially given the relatively large projected rotational velocities.

Recently multi-epoch spectroscopy has been obtained for 88 VFTS B-type binary candidates (Villaseñor et al. 2021). Binarity was confirmed in 64 targets corresponding to 73 per cent of the sample with 50 SB1 and 14 SB2 systems. For another 20 targets, designated as SB1*, clear signs of periodicity were identified but it was not possible to definitively confirm binarity. The remaining four targets showed evidence of radial velocity variations but not of periodicity and were designated as 'RV var'. In Fig. 7, the estimated semi-amplitudes (K_1) are plotted against the (uncorrected) $v_e \sin i$ -estimates.

For our six SB1 Be-type candidates, one (#874) was confirmed as an SB1 system, with the others being designated as SB1* (see Section 2.2 for details); their orbital parameters are summarized

Table 12. Parameters for the VFTS Be-type systems with orbital parameters taken from Villaseñor et al. (2021).

VFTS	P days	$\begin{array}{c} K_1 \\ kms^{-1} \end{array}$	e	$f(m)$ ${ m M}_{\odot}$
213	13.6	20.3	0.64	0.00536
337	25.5	37.9	0.55	0.08435
697	1.49	12.8	0.31	0.00029
847	1.23	26.7	0.50	0.00159
874	370.8	17.0	0.21	0.17616
877	94.7	8.8	0.32	0.00572

in Table 12. They have estimated periods from ~ 1 d to ~ 1 yr and eccentricities between 0.20 and 0.64 whilst their systemic radial velocities are consistent with the other B-type systems. The periods are smaller than have been found in Galactic B-type stars (Oudmaijer & Parr 2010; Rivinius et al. 2013) and may in part reflect the detection sensitivity for the VFTS sample, decreasing for periods, $P \gtrsim 100$ days. However the shortest period binaries may not be able to contain a Be-type disc within their Roche lobe (Rivinius et al. 2013; Lennon et al. 2021), implying that they may not be classical Be-type stars. It is also notable that all the Be-type systems have large eccentricities.

Inspection of Fig. 7 also shows that their estimated semi-amplitudes are all relatively low, with $K_1 < 40 \ \mathrm{km \, s^{-1}}$; by contrast Villaseñor et al. (2021) found 29 VFTS B-type systems (that have not been classified as supergiants), which had $K_1 > 40 \ \mathrm{km \, s^{-1}}$. The number of VFTS targets classified (Evans et al. 2015) as Be-type and B-type (excluding supergiants) were 69 and 310, respectively. Fischer and χ^2 tests returns a probability of <1 per cent that the Be-type and B-type samples have the same frequency of binary systems with $K_1 > 40 \ \mathrm{km \, s^{-1}}$. Hence we conclude that there is some evidence for a dearth of spectroscopic VFTS Be-type binaries, whilst those that are observed have significantly lower semi-amplitudes than those for the B-type binaries.

7 PRINCIPAL RESULTS AND IMPLICATIONS

The main results of our analysis are as follows:

- (i) For both of our samples, the $v_e \sin i$ -estimates of the Be-type are larger than those for normal B-type stars. The means for the former are typically 100 km s^{-1} larger than those for the latter.
- (ii) Monte Carlo simulations imply that for our Be-type samples, the mean ratio of the rotational velocity to the critical velocity is $\gamma_e \sim 0.7$.
- (iii) The de-convolution of the $v_e \sin i$ -estimates leads to mean v_e -estimates of 320–350 km s⁻¹ and 305–325 km s⁻¹ for the VFTS and NGC 346 samples, respectively. These are 100–150 km s⁻¹ larger than those for the corresponding B-type samples.
- (iv) The deconvolution of the $F_{\rm crit}$ estimates lead to $\gamma_{\rm e}$ -distributions that have a dearth of targets with $\gamma_{\rm e}{\lesssim}0.4$, with a broad distribution reaching up to critical rotation, $\gamma_{\rm e}{\simeq}1$. Our best estimate for the mean or median of the $\gamma_{\rm e}$ -values is 0.68, consistent with the Monte Carlo simulations. There is no evidence for any significant differences between the SMC and LMC samples, whilst these characteristics are very similar to those found by Zorec et al. (2016) and Balona & Ozuyar (2020a) for Galactic Be-type stars.
- (v) Rapidly rotating B-type stars appear to be as numerous as their Be-type counterparts. The ratio of the number of Be-type stars to B-type stars, R, is estimated as \sim 0.5–0.7 and \sim 1.0–1.5 for the VFTS and NGC 346 samples, respectively.

(vi) The frequency of Be-type stars identified as binary systems is lower than that for normal B-type stars. For the VFTS samples the semi-amplitudes for the former are also lower than those of the latter with a high level of significance, which is consistent with the differences in their radial velocity dispersions.

Below we discuss our results in the context of the current evolutionary models for the formation of Be-type stars. These fall into two main categories, viz. that Be-type star have evolved either as single stars or as multiple system with mass transfer (henceforth termed 'single' and 'binary'). The former, first suggested by Struve (1931), has been reviewed by Rivinius et al. (2013) with extensive modelling and population synthesis recently undertaken by Hastings et al. (2020). The latter has been discussed by Pols et al. (1991), de Mink et al. (2013), Shao & Li (2014, 2020), and Langer et al. (2020), and for example, is clearly relevant to Be/X-ray binaries (see for example, Raguzova & Popov 2005). Recently it has been invoked to explain the candidate intermediate mass black hole systems, LB1 and HR6819 (Bodensteiner et al. 2020c; Shenar et al. 2020; El-Badry & Quataert 2021) as Be-type stars plus a stripped helium star (henceforth characterized as Be/He binaries).

The wide range of γ_e -values found in Section 6.4 and illustrated in Fig. 5 provide a challenge for both evolutionary histories. For single star evolution, Hastings et al. (2020) find that reasonable agreement for the fraction of Be-type stars in the B-type population can be obtained if Be-type stars have γ_e -values in the range 0.7–0.8. The γ_e distributions illustrated in Fig. 5 imply that approximately 60 per cent of Be-type stars have $\gamma_e \ge 0.7$; scaling these distributions as discussed in Section 6.4 would reduce this percentage to ~48 per cent. However Hastings et al. (2020) assumed that all B-type stars with a γ_e value above a given threshold would exhibit Be-type phenomena and as discussed in Section 6.5, this is not the case. In order to produce sufficient Be-type stars would require a lowering of the γ_e threshold in their population synthesis. In turn this would lead to better agreement with the γ_e -distributions shown in Fig. 5. Hence given the uncertainties in both our results and the simulations of Hastings et al. (2020), our γ_e -distributions may be consistent with a single star evolutionary history.

Many authors (see for example, Pols et al. 1991; de Mink et al. 2013; Shao & Li 2014, 2020; Langer et al. 2020) have discussed the evolution of massive-star binaries until the primary becomes either a white dwarf, a stripped helium star, a neutron star, or a black hole. These simulations imply that the secondary's rotational velocity will increase due to the accretion of mass and angular momentum from the primary. There will also be mechanisms that 'spin-down' the secondary, with Shao & Li (2020) finding that tidal interactions are especially important. Langer et al. (2020) considered the evolution of binary system leading to a black hole and a massive main sequence star. For the latter, they deduced the probability distribution, $p(\gamma_e)$, which monotonically increased from $\gamma_e \sim 0.2$ up to unity; Be-type stars with neutron star or white dwarf companions would probably suffer less spin-down (Langer, private communication). As such, their γ_e -distribution would be shifted to higher values of γ_e , consistent with the observed Be-type stellar distribution shown in Fig. 5.

Very recently, Hastings et al. (2021) have investigated mass transfer interactions in B-type stars that could lead to Be-type secondaries. They focused on Be-type stars in clusters and deduced an expression for the fraction of Be-type to the total initial binary population in terms of the stellar mass compared with the turn-off mass of the cluster. They concluded that 'binary evolution does not allow more than around 30 per cent of stars to have been spun up

through binary interaction and become emission line objects'. For the VFTS sample, 73 Be-type stars have been identified out of a Btype population of 438 targets (Evans et al. 2015). Excluding the 52 B-type supergiants (which will normally have evolved from O-type progenitors) leads to 386 targets. Making the extreme assumption that the initial binary fraction, f, was unity would then lead to Be-type constituting 19 per cent of the binary population. Dunstall et al. (2015) estimated that the current binary fraction (allowing for unidentified systems) was $f = 0.55 \pm 0.11$ and this would increase the Be-type population to 28–43 per cent of the binaries. These latter percentages should be treated with caution because, as discussed by Hastings et al. (2021), the initial binary fraction and that currently observed may differ significantly. For NGC 346, the Be-type fraction of the total B-type population (again excluding supergiants) would be 23 per cent with the current binary fraction being poorly constrained. Hence the frequency of Be-type stars within our samples are consistent with the simulations of Hastings et al. (2021). However, Bodensteiner et al. (2020a) find a lower limit on the Be-type stellar fraction of \sim 32 per cent in the older SMC cluster NGC 330, which is larger than the predictions of Hastings et al. (2020)

Bodensteiner et al. (2020b) investigated a sample of 287 Galactic early-Be-type targets and concluded that there were 'no confirmed reports of Be binaries with MS companions' and that the Galactic sample 'strongly supports the hypothesis that early-type Be stars are binary interaction products that spun up after mass and angular momentum transfer from a companion star'. However their analysis was complicated by the possibility of significant biases, which they characterized as the 'vast heterogeneity of techniques, data quality, and focus' of their sample. Recently Bodensteiner et al. (2021) have investigated binarity for B-type stellar population in the SMC cluster NGC 330 and again found a smaller observed fraction amongst the Be-type stars. These analyses are consistent with the dearth of spectroscopic binaries found in the VFTS Be-type sample discussed in Section 6.6.

From the above discussion, it is not possible to conclude definitively that our Be-type samples are produced predominantly through one evolutionary pathway. The wide range of γ_e -values found in both of our samples (and indeed in other studies) requires a mechanism that leads to targets which have *currently* relatively low γ_e -values. If Be-type stars were the products of binary evolution, the substantial populations of rapid rotating B-type stars could then be due to the latter being single stars. Additionally recent modelling of binary populations is consistent with the observed number of Be-type stars in our sample. Assuming that one mechanism did dominate the production of classical Be-type stars, our results would favour a binary evolutionary history.

ACKNOWLEDGEMENTS

We are grateful to Michael Abdul-Masih, Nate Bastian, Julia Bodensteiner, Ben Hastings, Norbert Langer, Fabian Schneider, and Jorick Vink for useful discussions. The paper has also benefited from constructive comments from the referee. Based on observations at the European Southern Observatory Very Large Telescope in programmes 171.D-0237171.0237, 182.D-0222, and 096.D-0825 and on observations made with the NASA/ESA *Hubble Space Telescope*, and obtained from the Hubble Legacy Archive, which is a collaboration between the Space Telescope Science Institute (STScI/NASA), the Space Telescope European Coordinating Facility (ST-ECF/ESA), and the Canadian Astronomy Data Centre (CADC/NRC/CSA).

DATA AVAILABILITY

The spectroscopic data were obtained during ESO programmes, 171.D-0237171.0237, 182.D-0222 and 096.D-0825. Data products are available from the ESO Science Archive Portal (https://archive.eso.org/scienceportal/home). Spectra are available at http://www.roe.ac.uk/~cje/tarantula/spectra, https://star.pst.qub.ac.uk/~sjs/flames/, or on request from the authors.

REFERENCES

Abdul-Masih M., Sana H., Conroy K. E., Sundqvist J., Prša A., Kochoska A., Puls J., 2020, A&A, 636, A59

Ahmed A., Sigut T. A. A., 2017, MNRAS, 471, 3398

Balona L. A., Ozuyar D., 2020, MNRAS, 493, 2528

Balona L. A., Ozuyar D., 2021, ApJ, 921, 5

Barraza L. F. et al., 2022, ApJ, 924, 117

Bastian N. et al., 2017, MNRAS, 465, 4795

Bodensteiner J. et al., 2020a, A&A, 634, A51

Bodensteiner J., Shenar T., Sana H., 2020b, A&A, 641, A42

Bodensteiner J. et al., 2020c, A&A, 641, A43

Bodensteiner J. et al., 2021, A&A, 652, A70

Carroll J. A., 1933, MNRAS, 93, 478

Collins George W. I., 1987, in Slettebak A., Snow T. P., eds, IAU Colloq.92: Physics of Be Stars, Cambridge University Press, Cambridge, p. 3,

Collins G. W. I., Sonneborn G. H., 1977, ApJS, 34, 41

Collins G. W. I., Truax R. J., Cranmer S. R., 1991, ApJS, 77, 541

Cranmer S. R., 2005, ApJ, 634, 585

de Mink S. E., Langer N., Izzard R. G., Sana H., de Koter A., 2013, ApJ, 764, 166

Dufton P. L., Ryans R. S. I., Simón-Díaz S., Trundle C., Lennon D. J., 2006, A&A, 451, 603

Dufton P. L. et al., 2013, A&A, 550, A109

Dufton P. L., Evans C. J., Hunter I., Lennon D. J., Schneider F. R. N., 2019, A&A, 626, A50

Dunstall P. R., Brott I., Dufton P. L., Lennon D. J., Evans C. J., Smartt S. J., Hunter I., 2011, A&A, 536, A65

Dunstall P. R. et al., 2015, A&A, 580, A93

El-Badry K., Quataert E., 2021, MNRAS, 502, 3436

Evans C. J. et al., 2011, A&A, 530, A108

Evans C. J. et al., 2015, A&A, 574, A13

Evans C. J., Lennon D. J., Smartt S. J., Trundle C., 2006, A&A, 456, 623 Fasano G., Franceschini A., 1987, MNRAS, 225, 155

Fraser M., Dufton P. L., Hunter I., Ryans R. S. I., 2010, MNRAS, 404, 1306 Frémat Y., Zorec J., Hubert A.-M., Floquet M., 2005, A&A, 440, 305

Garland R. et al., 2017, A&A, 603, A91

Gray D. F., 2005, The Observation and Analysis of Stellar Photospheres, 3 edn. Cambridge Univ. Press, Cambridge

Griem H. R., 1997, Principles of Plasma Spectroscopy. Cambridge Monographs on Plasma Physics, Cambridge Univ. Press, Cambridge

Hastings B., Wang C., Langer N., 2020, A&A, 633, A165

Hastings B., Langer N., Wang C., Schootemeijer A., Milone A. P., 2021, A&A, 653, A144

Hoffleit D., Jaschek C., 1991, The Bright Star Catalogue. Yale University Observatory, New Haven

Jaschek C., Jaschek M., 1990, Classification of Stars, Cambridge University Press, Cambridge

Kramida A., Yu. Ralchenko Reader J., NIST ASD Team, 2018, NIST Atomic Spectra Database (ver. 5.6.1), National Institute of Standards and Technology, Gaithersburg, MD,

Labadie-Bartz J., Carciofi A. C., de Amorim T. H., Rubio A., Luiz A., Ticiani dos Santos P., Thomson-Paressant K., 2020, preprint (arXiv:2010.13905)

Langer N. et al., 2020, A&A, 638, A39

Lefever K., Puls J., Aerts C., 2007, A&A, 463, 1093

Lennon D. J., Dufton P. L., Villaseñor J. I., Evans C. J., Langer N., Saxton R., Monageng I. M., Toonen S., 2021, preprint (arXiv:2111.12173)

Liu J. et al., 2019, Nature, 575, 618

Lucy L. B., 1974, AJ, 79, 745

McEvoy C. M. et al., 2015, A&A, 575, A70

Markova N., Puls J., 2008, A&A, 478, 823

Martayan C., Hubert A. M., Floquet M., Fabregat J., Frémat Y., Neiner C., Stee P., Zorec J., 2006, A&A, 445, 931

Martayan C., Frémat Y., Hubert A.-M., Floquet M., Zorec J., Neiner C., 2007a, A&A, 462, 683

Martayan C., Floquet M., Hubert A. M., Gutiérrez-Soto J., Fabregat J., Neiner C., Mekkas M., 2007b, A&A, 472, 577

Miodrag L., 2011, International Encyclopedia of Statistical Science, 1 edn., Springer-Verlag, Berlin/Heidelberg

Oudmaijer R. D., Parr A. M., 2010, MNRAS, 405, 2439

Pasquini L. et al., 2002, Messenger, 110, 1

Patrick L. R. et al., 2019, A&A, 624, A129

Pols O. R., Cote J., Waters L. B. F. M., Heise J., 1991, A&A, 241, 419

Raguzova N. V., Popov S. B., 2005, Astron. Astrophys. Trans., 24, 151

Ramírez-Agudelo O. H. et al., 2013, A&A, 560, A29

Ramírez-Agudelo O. H. et al., 2015, A&A, 580, A92

Rivinius T., Carciofi A. C., Martayan C., 2013, A&AR, 21, 69

Rivinius T., Baade D., Hadrava P., Heida M., Klement R., 2020, A&A, 637, L3

Sana H. et al., 2013, A&A, 550, A107

Schneider F. R. N. et al., 2018, Science, 359, 69

Shao Y., Li X.-D., 2014, ApJ, 796, 37

Shao Y., Li X.-D., 2020, ApJ, 898, 143

Shenar T. et al., 2020, A&A, 639, L6

Simón-Díaz S., Herrero A., 2007, A&A, 468, 1063

Simón-Díaz S., Herrero A., 2014, A&A, 562, A135

Simón-Díaz S., Herrero A., Uytterhoeven K., Castro N., Aerts C., Puls J., 2010, ApJ, 720, L174

Simón-Díaz S., Godart M., Castro N., Herrero A., Aerts C., Puls J., Telting J., Grassitelli L., 2017, A&A, 597, A22

Simón-Díaz S. et al., 2020, A&A, 634, L7

Struve O., 1931, ApJ, 73, 94

Takeda Y., Kawanomoto S., Ohishi N., 2017, MNRAS, 472, 230

Townsend R. H. D., Owocki S. P., Howarth I. D., 2004, MNRAS, 350, 189

Villaseñor J. I. et al., 2021, MNRAS, 507, 5348 Zorec J., Briot D., 1997, A&A, 318, 443

Zorec J. et al., 2016, A&A, 595, A132

SUPPORTING INFORMATION

Supplementary data are available at *MNRAS* online.

Table S1. Differences between the $v_e \sin i$ estimates from individual He I lines and the means summarized in Table 2.

Table S2. Comparison of the projected rotational velocity estimates obtained from the two line-sets.

Table S3. Statistics for the stochastic uncertainties in the $v_e \sin i$ estimates.

Table S4. Differences between the v_r estimates from individual He I lines and the means summarized in Table 2.

Table S5. Comparison of the radial velocity estimates obtained from the two line-sets.

Figure S1. Observed and theoretical profiles for #034.

Figure S2. Projected rotational velocities found by Dufton et al. (2013) and Garland et al. (2017) plotted against our current FT estimates.

Figure S3. Observed and theoretical profiles for #034.

Figure S4. Observed and theoretical profiles for #298.

Please note: Oxford University Press is not responsible for the content or functionality of any supporting materials supplied by the authors. Any queries (other than missing material) should be directed to the corresponding author for the article.

This paper has been typeset from a TEX/LATEX file prepared by the author.